



# PhD Thesis

PhD Thesis

PhD Thesis

**by Niclas Lars Rudolf Fiedler, M.Sc.**  
from Weilmünster  
XX.XX.2028

Justus Liebig University Gießen  
Institute of Experimental Physics II

First Examiner: Prof. Dr. Kai-Thomas Brinkmann  
Second Examiner: Prof. Dr. Jens Sören Lange, AkR  
Supervisor: Dr. Dzmitry Kazlou



## **Abstract**

## **Zusammenfassung**

# **Contents**

# Chapter 1

## Detector Design and Construction

### 1.1 Introduction & Motivation

### 1.2 Detector Concept & Scintillator Selection

Two different scintillation-based detector-concepts were developed to measure the depth dose distribution of protons in real-time. Both detectors consist of 32 scintillator-layers read-out via Silicon PhotoMultipliers (SiPMs) and two linked-together 16-channel CAEN digitizers.

The first detector concept is PbWO<sub>4</sub>-based, as the first prototype, [citemaster], but improves on the layer geometry by using sheets instead of bars whilst also reducing layer thickness. For this two crystal sizes were chosen with  $30 \times 30 \times 3 \text{ mm}^3$  and  $30 \times 30 \times 2 \text{ mm}^3$ , which were provided and cut by Crytur, allowing full coverage of the 220 MeV proton range of  $\approx 66 \text{ mm}$ . The lateral sheet sizes with 30 mm were the largest provable, as the sheets were cut from a single ingot with a fixed size. The 3 mm thick sheets are used in the front or shallow beam depths to provide more stopping power and the thinner 2 mm sheets are used in the Bragg-Peak region to give an optimal spatial resolution.

The second detector concept using plastic scintillators was developed to further increase the spatial resolution in the Bragg-Peak region at the cost of dynamic range in the shallow depths. Plastic scintillators were chosen because they have a much lower density and thereby stopping power than PbWO<sub>4</sub> and a high light yield also giving a better energy

resolution. However, to achieve a high spatial resolution whilst using only 32 channels, individual channels need a low radiological thickness resulting in not fully covering the proton range. To still stop the proton beam, a passive absorber with a known stopping power i.e. radiological thickness is incorporated between the first and second scintillator layers. This allows the first to work as a trigger channel which is used for the normalization in the analysis.

## 1.3 Detector Simulation

Geant4 simulations of both detector designs were implemented to give insights into their respective performances and to strike a good balance between active and passive volume for the plastic based detector. For this the reference physics list QGSP\_BIC\_EMY was chosen with the addition of substituting G4EmStandardPhysics\_option3 with G4EmStandardPhysics\_option4. The production cut was uniformly set to 0.05 mm for all particle types, which corresponds to an energy threshold of approximately 55 keV for electrons in water [**<empty citation>**] (baumann2017). This threshold defines the minimum range a secondary particle must have to be explicitly generated in the simulation; particles with shorter ranges deposit their energy locally without being tracked as individual secondaries.

### 1.3.1 Detector Implementation

The PbWO<sub>4</sub>-based detector was implemented as 32 PbWO<sub>4</sub> sheets with the dimensions from Section ???. The mean excitation energy was set to 600.7 eV (citation needed), Birks' Coefficient to 0.008694  $\frac{\text{MeV}}{\text{cm}}$ , the absorption length to 100 cm, the lightyield to 200 ph/MeV and the refractive index to 2.2 (citation). The crystals are wrapped in 0.25 mm PTFE-foil and 20  $\mu\text{m}$  aluminum foil per side, as measured in Section ?? (reference needed). Here PTFE is modeled after its molecular formula of the repeating unit C<sub>2</sub>F<sub>4</sub> with a density of  $\rho_{\text{PTFE}} = 2.2 \frac{\text{g}}{\text{cm}^3}$  and a mean excitation energy of  $I_{\text{PTFE}} = 99.1 \text{ eV}$  [citation needed] and the aluminum foil (99.9 %) is approximated by solid aluminum. The scintillators are wrapped in 0.5 mm PTFE-foil and 20  $\mu\text{m}$  aluminum foil. Here PTFE is modeled after its molecular formula of the repeating unit C<sub>2</sub>F<sub>4</sub> with a density of  $\rho_{\text{PTFE}} =$

$2.2 \frac{\text{g}}{\text{cm}^3}$  and a mean excitation energy of  $I_{\text{PTFE}} = 99.1 \text{ eV}$  [citationneeded] and the aluminum foil (99.9 %) is approximated by aluminum.

The plastic based detector was implemented using an active and passive material. The active material was modeled after a PVT-based scintillator, similar to general purpose plastic scintillators like EJ-200 or BC-408. Here, the material is composed out of hydrogen and carbon with the mass fractions of 8.5 % and 91.5 %, respectively [citeEJ]. The passive material is PMMA and modeled after its molecular formula of the repeating unit  $\text{C}_5\text{H}_8\text{O}_2$  with a density of  $\rho_{\text{PMMA}} = 1.9 \frac{\text{g}}{\text{cm}^3}$  and a mean excitation energy of  $I_{\text{PMMA}} = 74 \text{ eV}$  [citationneeded]. Here, the scintillators are again wrapped in PTFE and aluminum foil.

From Equation ?? follows that a 220 MeV proton beam has a range of 30.45 cm in water. Considering that plastic scintillators have a very similar stopping power and that the Bragg-Peak region is about 1/3 of the depth-dose distribution this leads to a scintillator thickness of  $\approx 4 \text{ mm}$ . For the 32 available channels this gives a coverage of  $\approx 12.8 \text{ cm}$  of the 30.45 cm proton range, resulting in a  $\approx 20 \text{ cm}$  passive absorber. To chose the right thickness of the PMMA absorber, its water equivalent radiological thickness after the first scintillator layer has to be calculated. This is done using the total energy deposition inside the absorber by integrating Equation ??(range energy), as shown in Equation ??.

$$\Delta E_{\text{H}_2\text{O}} = \Delta E_{\text{mat}} \quad (1.1)$$

$$\int_{z_n}^{z_{n+1}} S_{\text{H}_2\text{O}} dz = \int_{x_n}^{x_{n+1}} S_{\text{mat}} dx \quad (1.2)$$

$$E(z_{n+1})_{\text{H}_2\text{O}} - E(z_n)_{\text{H}_2\text{O}} = E(x_{n+1})_{\text{mat}} - E(x_n)_{\text{mat}} \quad (1.3)$$

$$E(z_n)_{\text{H}_2\text{O}} = E(x_n)_{\text{mat}} \rightarrow E(z_{n+1})_{\text{H}_2\text{O}} = E(x_{n+1})_{\text{mat}} \quad (1.4)$$

$$x_{n+1} = x_n + \Delta x \rightarrow \left( \frac{z_{n+1}}{\alpha_{\text{H}_2\text{O}}} \right)^{\frac{1}{p_{\text{H}_2\text{O}}}} = \left( \frac{x_n + \Delta x}{\alpha_{\text{mat}}} \right)^{\frac{1}{p_{\text{mat}}}} \quad (1.5)$$

$$x_n = \alpha_{\text{mat}} \left( \frac{z_n}{\alpha_{\text{H}_2\text{O}}} \right)^{\frac{p_{\text{mat}}}{p_{\text{H}_2\text{O}}}} \rightarrow z_{n+1} = \alpha_{\text{H}_2\text{O}} \left( \left( \frac{z_n}{\alpha_{\text{H}_2\text{O}}} \right)^{\frac{p_{\text{mat}}}{p_{\text{H}_2\text{O}}}} + \frac{\Delta x}{\alpha_{\text{mat}}} \right)^{\frac{p_{\text{H}_2\text{O}}}{p_{\text{mat}}}} \quad (1.6)$$

using  $z_0 = x_0 = 0$ .

## 1.4 Readout

The scintillators of both designs are read out via SiPMs. Light yield measurements were conducted, to decide which SiPM types are suitable. With these the amount of incident photons can be estimated and compared with the number of pixel. From this, a balance can be struck between high resolution and a large enough dynamic range.

## 1.5 Detector Housing

The scintillators are held in place by a custom 3D-printed PLA housing, as shown in Figure ??(fig needed). The crystals are spaced 6.6 mm center-to-center, leaving 3 mm of space inbetween for calibration sources. Small crevices on the top side allow for easy insertions of sources using the custom 3D-printed holder shown in Figure ???. X-shaped springs are 3D-printed out of flexible TPU, shown in Figure ??, and used to create slight pressure between the scintillators and the SiPMs for optimal optical coupling. The springs are moved using screws and heat-set threaded inserts as shown in Figure ???. Markings on each side indicate the correct beam alignment.

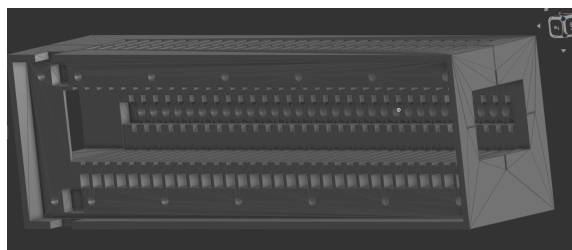
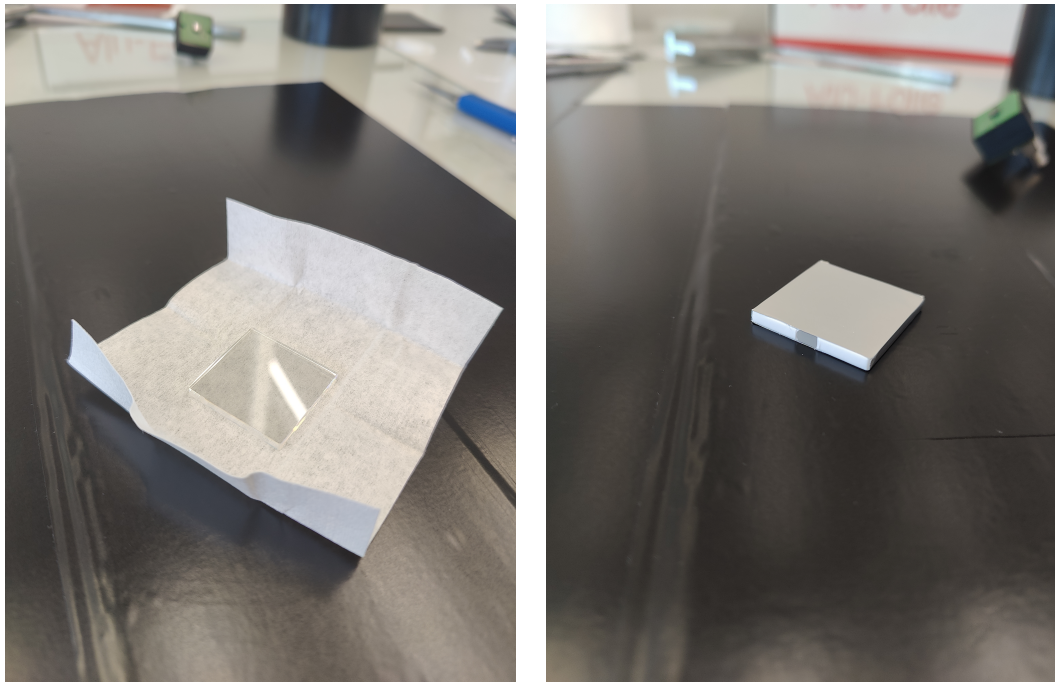


Figure 1.1: Caption

### 1.5.1 Wrapping

The crystals were wrapped in a high-reflectivity PTFE membrane to increase the light yield and decrease the cross-talk probability. For this the crystals are first cleaned with ethanol, as shown in Figure ???. Then they are tightly wrapped in three layers of PTFE

membrane, with an SiPM-sized window cut-out on one side where the SiPM will be attached, as shown in Figure ???. The PTFE-membrane is the Tetratex® ePTFE-membrane with 127  $\mu\text{m}$  membrane thickness at a density of 0.35 g/cm<sup>3</sup> [1]. It reflects the scintillation light back inside the crystal so that it can only exit the crystal on the open side where the SiPM is located. The wrapped crystals are additionally wrapped tightly in one layer of 20  $\mu\text{m}$  [1] aluminum foil, fixated using reflective tape, as shown in Figure ???. This protects the wrapping and ensures light-tightness from both inside and outside. Its reflectiveness helps redirect any remaining light that might pass through the PTFE, particularly on the edges and corners where the wrapping is thinnest.



(a) Cleaned PbWO<sub>4</sub> crystal.

(b) Fully wrapped PbWO<sub>4</sub> crystal with window cut-out.

## 1.5.2 Light Yield Measurement

The measurements were conducted using the process described in Section ?? and the setup shown in Figure ???. The PMT used is an R2059 from Hamamatsu (serial number BA3200) with a quantum efficiency of 23.16 % [2] (cf. Appendix ??) at the luminescence

peak of 420 nm of PbWO<sub>4</sub> [3] and EJ212.

### 1.5.2.1 Light Yield: PbWO<sub>4</sub>

The PbWO<sub>4</sub> measurement were done in a flat and vertical position as shown in Figure ??, where all non PMT-facing scintillator sides were enveloped in highly reflective PTFE foil in order to not lose any photons. Two additional measurements were performed, where one 3 mm- and 2 mm crystal were fully wrapped with an SiPM sized window cutout in the center of one side as shown in Figure ?? . The PbWO<sub>4</sub> crystals were mounted onto the PMT's optical window next to a <sup>22</sup>Na  $\gamma$ -source inside a climate chamber. The optical coupling was done using glycerol ( $n = 1.4722$ ), as shown in Figure ?? . Glycerin was used as a substitute for the commonly used Baysilone® Fluid M optical grease ( $n \approx 1.404$ ,  $\eta = 300\,000\text{mm}^2/\text{s}$  [4]), due to its less-adhesive characteristic. The Baysilone® Fluid M with its high adhesion might have lead to damaging the fragile crystals during removal. The refractive index of PbWO<sub>4</sub> and the SiO<sub>2</sub> glass window of the PhotoMultiplier Tube (PMT) are  $n_{\text{PbWO}_4} \approx 2.3$  [3] and  $n_{\text{SiO}_2} \approx 1.459$  [5], respectively. Additionally to the climate chamber's light-tightness, the setup is enclosed in PTFE foil, ensuring perfect light tightness.

The measurements were conducted at 20 °C for 5 min after an acclimation time of 5 min each. The acclimation time was chosen small because the crystals were kept inside the climate chamber for 24 h before the measurements were startet, thereby only the short time frame inbetween measurements, where the chamber was opened, had to be accounted for. An exemplary light yield measurement of crystal number 0 in the flat position is shown in Figure ?? . The measured light yield values of all crystals and their averages for the different setups are shown in Figure ?? . The 3 mm thick crystals average approximately 164.73 ph/MeV and 129.44 ph/MeV in the flat and vertical positions, respectively. The 2 mm thick crystals average approximately 131.00 ph/MeV and 94.32 ph/MeV in the flat and vertical positions, respectively. With the SiPM-sized window cutout the light yield of a 3 mm and 2 mm crystal was  $(75.25 \pm 33.09)$  ph/MeV and  $(59.70 \pm 19.22)$  ph/MeV, respectively.

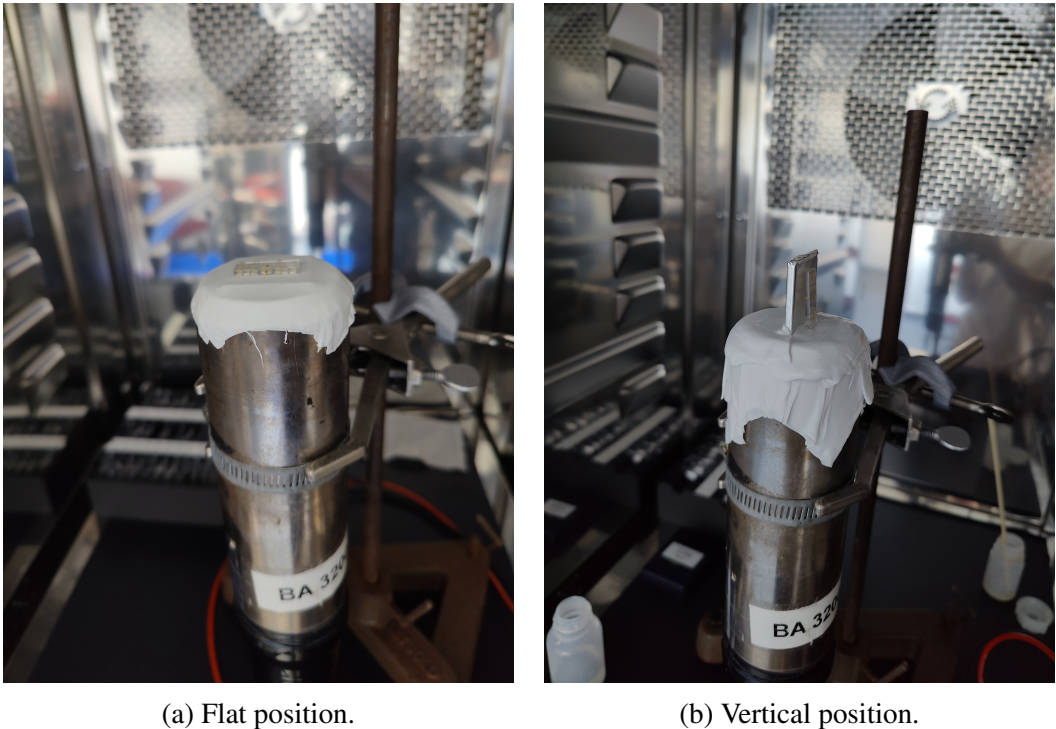


Figure 1.3: Measurement positions of the  $\text{PbWO}_4$  scintillators on the PMT for the light yield measurements using a  $^{22}\text{Na}$  source.

### 1.5.2.2 Light Yield: EJ-200

The light yield of a  $50 \times 50 \times 10 \text{ mm}^3$  EJ-200 sample was measured to estimate the amount of incident photons on an SiPM optically coupled to an EJ-212 scintillator, which has similar properties to EJ-200, to decide which SiPM type is needed for the readout.

The measurements were done in a flat and vertical position, with two source positions for the vertical setup, as shown in Figure ???. In the vertical position two wrappings for the scintillator were used. First the whole PMT facing side was left open and secondly only an SiPM-sized window cutout was left open. The scintillator was mounted onto the PMT's optical window inside a climate chamber and optically coupled using Baysilone<sup>®</sup> Fluid M optical grease [4]. The setups were fully enclosed in PTFE foil to ensure light-tightness. The source positions were on the side and on top of the scintillator. A  $^{241}\text{Am}$  source was chosen due to the high light yield of EJ200 as  $^{241}\text{Am}$  has a prominent low-energy gamma line at 59.6 eV.

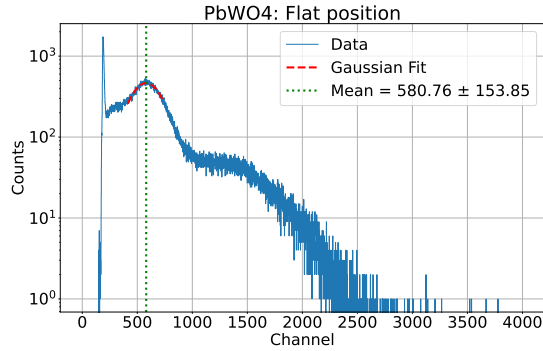


Figure 1.4: Example light yield measurement of the 3 mm thick PbWO<sub>4</sub>-crystal number 0 in flat position on the PMT using a <sup>22</sup>Na source.

The measurements were conducted at 20 °C for 20 min after an acclimation time of 24 h. The measurements and Gaussian fits of the 59.6 eV peak are shown in Figure ??.

The light yield results are shown in Table ?? . The light yield for the flat position is in good agreement with the value provided by the manufacturer of 10 000 ph/MeV, taking into account aging-related degradation of the PMT (from 2012), which reduce the quantum efficiency. For both vertical positions, the light yield is only slightly affected by the source position. This is due to the high attenuation length of optical photons in the scintillator of 380 cm. When photons are collected from one side, approximately 30 % of the total light is lost and when using an SiPM-sized window cut-out the light yield is reduced by 70 %.

Measurement	Peak position / ADC	Light yield / $\frac{\text{p.e.}}{\text{MeV}}$	Light yield / $\frac{\text{ph}}{\text{MeV}}$
Flat	$3065.69 \pm 450.48$	$1996.24 \pm 301.74$	$8619.36 \pm 1302.84$
Vertical, Top	$2110.67 \pm 330.26$	$1356.56 \pm 221.21$	$5857.33 \pm 955.15$
Vertical, Side	$2196.13 \pm 362.80$	$1413.80 \pm 243.01$	$6104.49 \pm 1049.26$
Vertical, Window, Top	$948.9 \pm 210.69$	$578.39 \pm 141.12$	$2497.35 \pm 609.34$
Vertical, Window, Side	$975.01 \pm 241.14$	$595.87 \pm 161.52$	$2572.86 \pm 697.41$

Table 1.1: Light yield measurement results of the 50 × 50 × 10mm<sup>3</sup> EJ-200 scintillator sample.

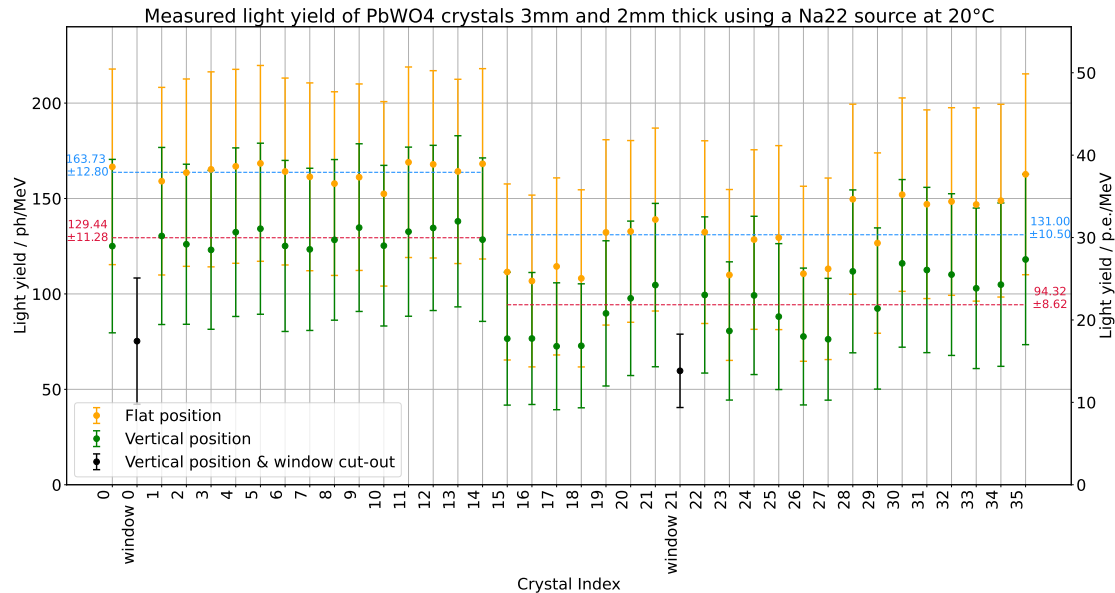


Figure 1.5: Light yield measurements of  $\text{PbWO}_4$ -crystals in flat and vertical positions including two window cut-out measurements using a  $^{22}\text{Na}$  source.

## 1.6 Photon Readout and SiPM Selection

An optimal SiPM-type for measuring the proton depth-dose distribution for the given scintillators needs to balance a high resolution with a high dynamic range to accurately measure the low energies in the shallow depths and the high energies in the Bragg-Peak region. To ensure a linear SiPM signal, the number of impinging photons needs to be less or equal to approximately 10 % of the number of pixels divided by the Photo-Detection Efficiency (PDE).

### 1.6.1 SiPM for $\text{PbWO}_4$

The light yield measurements of the teflon-wrapped  $\text{PbWO}_4$  crystals with an SiPM-sized window cutout resulted in  $(75.25 \pm 33.09)$  ph/MeV and  $(59.70 \pm 19.22)$  ph/MeV for the 3 mm and 2 mm thick crystal, respectively. The SiPM-type chosen, was the already available Broadcom AFBR-S4N44P014M, with an active area of  $3.72 \times 3.62 \text{ mm}^2$ , a micro cell pitch of  $40 \mu\text{m}$ , 8334 microcells and a maximum PDE of 63 % at 420 nm coinciding

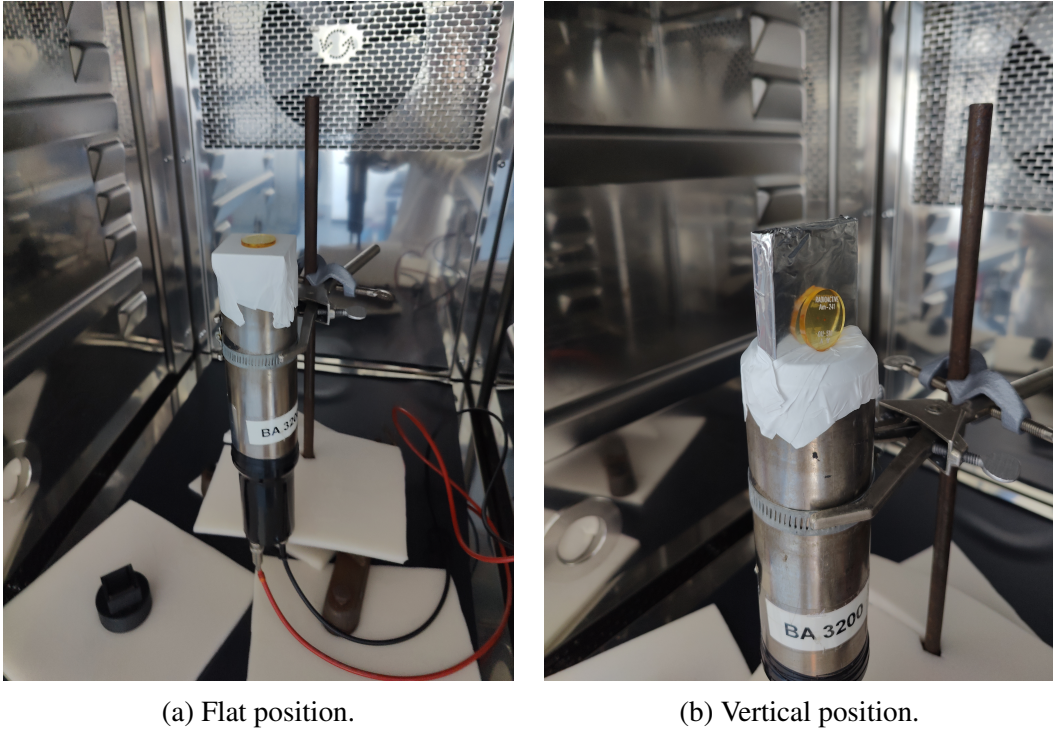


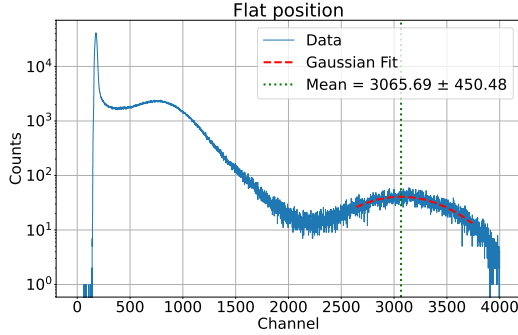
Figure 1.6: Measurement positions of the EJ-200 scintillator on the PMT for the light yield measurements using a  $^{241}\text{Am}$  source.

with the luminescence maximum of  $\text{PbWO}_4$ . The upper limit of the expected number of triggered pixels can be calculated using the highest simulated energy loss in the Bragg-Peak region, which is approximately 40 MeV, as shown in Figure ???. Accounting for the covered active area of the SiPM by the 2 mm thick crystal gives:

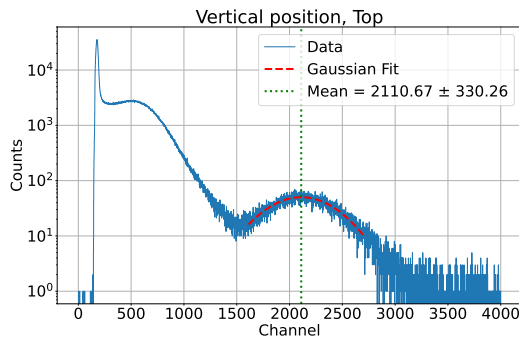
$$\frac{N(E)}{N(A)} = E \cdot \frac{L \cdot PDE}{N_0 \frac{A_{cov}}{A_{SiPM}}} \quad (1.7)$$

$$\frac{N(E_{max} = 40 \text{ MeV})}{N(A)} = 40 \text{ MeV} \cdot \frac{59.7 \text{ ph/MeV} \cdot 0.63 \frac{1}{\text{ph}}}{N_0 \cdot \frac{2 \cdot 3.72 \text{ mm}^2}{3.62 \cdot 3.72 \text{ mm}^2}} \quad (1.8)$$

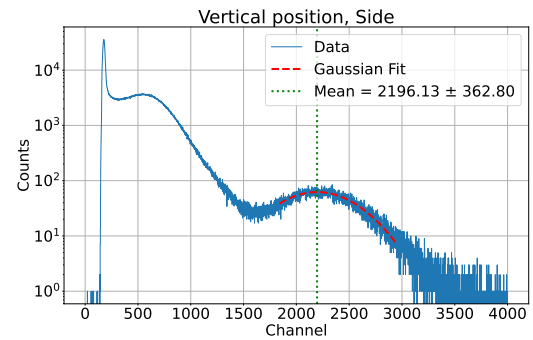
$$= 0.327 \quad (1.9)$$



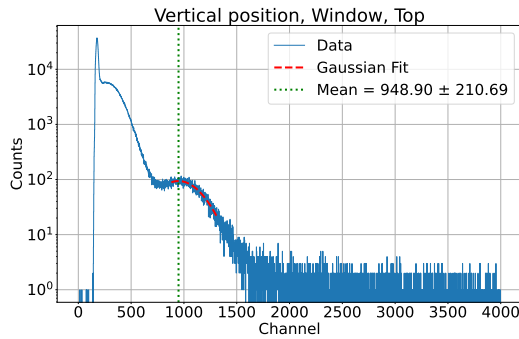
(a) Flat scintillator position.



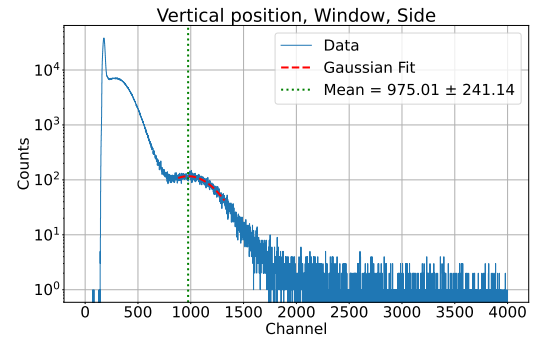
(b) Vertical position with open side and source on top.



(c) Vertical position with open side and source on the side.



(d) Vertical position with SiPM-sized window cutout and source on top.



(e) Vertical position with SiPM-sized window cutout and source on the side.

Figure 1.7: Light yield measurements of the  $50 \times 50 \times 10\text{mm}^3$  EJ-200 scintillator sample. Shown are the measurements of the scintillator in a flat position with a completely open side (??), in a vertical position with open side and the source on top (??) and on the side (??), and in a vertical position with an SiPM-sized window cutout with the source on top (??) and on the side (??).

## 1.6.2 SiPM for EJ-212

Since EJ-200 and EJ-212 are very similar the SiPM-type for the EJ-212 scintillators was chosen based on the measurements of EJ-200. The measured light yield for the teflon-wrapped EJ-200 scintillator with an SiPM-sized cut-out with a center positioned source is 2572.86 , as shown in Table ???. Due to the high light yield an SiPM, the Hamamatsu S14160-3010PS was chosen. This SiPM has an active area of  $3 \times 3\text{mm}^2$ , a micro cell pitch of  $10\text{\mu m}$ , 89984 microcells and a maximum PDE of 18 % at 460 nm, which is close to the luminescence maximum of EJ<sub>212</sub> at 423 nm. The upper limit of the expected number of triggered pixels is again calculated using the highest simulated energy loss in the Bragg-Peak region, which is approximately 20 MeV, as shown in Figure ???. Accounting for the fully covered active area of the SiPM this gives:

$$\frac{N(E)}{N_0} = E \cdot \frac{L \cdot PDE}{N_0} \quad (1.10)$$

$$\frac{N(E_{max} = 20\text{MeV})}{N(A)} = 20\text{MeV} \cdot \frac{2572.86\text{ph/MeV} \cdot 0.18\frac{1}{\text{ph}}}{N_0} \quad (1.11)$$

$$= 0.103 \quad (1.12)$$

## **1.7 Detector Assembly and Construction**

## **1.8 Experimental Setup**

## **1.9 Data Analysis**

## **1.10 Results**

## **1.11 Discussion**

## **1.12 Outlook**

### 1.12.0.1 Depth Calculation

In particle therapy, the measurement depth  $z$  in a detector is conventionally expressed as the water-equivalent thickness (WET). The WET  $t$  of a material layer is the thickness of water that causes the same energy loss for a proton beam. For this, the physical depth of the detector must be converted to a WET, allowing for direct comparisons.

The conversion is calculated by approximating the stopping power ratio of PbWO<sub>4</sub> and H<sub>2</sub>O, through the energy-range relation bortfeld at the nominal beam energy of 221.6 MeV.

$$t = \frac{S_{\text{PbWO}_4}}{S_{\text{H}_2\text{O}}} \cdot x = \frac{\frac{dE_{\text{PbWO}_4}}{dx}}{\frac{dE_{\text{H}_2\text{O}}}{dx}} \cdot x = \frac{\frac{1}{\alpha_{\text{PbWO}_4} \cdot p_{\text{PbWO}_4}} E^{1-p_{\text{PbWO}_4}}}{\frac{1}{\alpha_{\text{H}_2\text{O}} \cdot p_{\text{H}_2\text{O}}} E^{1-p_{\text{H}_2\text{O}}}} \cdot x = \frac{\alpha_{\text{H}_2\text{O}} \cdot p_{\text{H}_2\text{O}} E^{1-p_{\text{PbWO}_4}}}{\alpha_{\text{PbWO}_4} \cdot p_{\text{PbWO}_4} E^{1-p_{\text{H}_2\text{O}}}} \cdot x \quad (1.13)$$

##### Anfang alternativerer komplexerer Gleichung (braucht vielleicht noch Simulationsvalidierung, vielleicht was für ein anderes Paper)

The conversion is calculated iteratively for each material layer of the detector (e.g. wrapping, crystal), starting from the beam entrance. By definition, a proton's energy after traversing a depth  $t$  in water is identical to its energy after traversing a depth  $x$  in another material, where  $t$  is the WET corresponding to  $x$ . Using the empirical range-energy relationship for protons in matter bortfeld, the conversion of a materials depth  $x$  to WET  $t$  can be expressed as

$$E(t)_{\text{H}_2\text{O}} = E(x)_{\text{mat}} \quad (1.14)$$

$$\left( \frac{t}{\alpha_{\text{H}_2\text{O}}} \right)^{\frac{1}{p_{\text{H}_2\text{O}}}} = \left( \frac{x}{\alpha_{\text{mat}}} \right)^{\frac{1}{p_{\text{mat}}}} \quad (1.15)$$

$$t = \alpha_{\text{H}_2\text{O}} \left( \frac{x}{\alpha_{\text{mat}}} \right)^{\frac{p_{\text{H}_2\text{O}}}{p_{\text{mat}}}}, \quad (1.16)$$

where  $\alpha$  and  $p$  are the material-dependent parameters of the range–energy relation. In this formulation,  $p$  is assumed to be largely energy independent.

To extend this formalism to a detector consisting of multiple layers of different materials, an iterative approach is used. The cumulative WET after  $n$  layers,  $t_n$ , is calculated from

the WET after  $n - 1$  layers,  $t_{n-1}$ , and the physical thickness of the current layer  $\Delta x$ . The corresponding physical depth after  $n$  layers is given by

$$x_n = x_{n-1} + \Delta x. \quad (1.17)$$

By inserting  $x_n$  into  $t_n$  of Equation ??, and expressing  $x_{n-1}$  in terms of  $t_{n-1}$ , the WET can be calculated iteratively as

$$t_n = \alpha_{\text{H}_2\text{O}} \left( \frac{x_{n-1} + \Delta x}{\alpha_{\text{mat}}} \right)^{\frac{p_{\text{H}_2\text{O}}}{p_{\text{mat}}}} \quad (1.18)$$

$$t_n = \alpha_{\text{H}_2\text{O}} \left[ \left( \frac{t_{n-1}}{\alpha_{\text{H}_2\text{O}}} \right)^{\frac{p_{\text{mat}}}{p_{\text{H}_2\text{O}}}} + \frac{\Delta x}{\alpha_{\text{mat}}} \right]^{\frac{p_{\text{H}_2\text{O}}}{p_{\text{mat}}}}, \quad (1.19)$$

with the boundary conditions  $t_0 = 0$  and  $x_0 = 0$  at the detector entrance.

##### Ende von iterativer Gleichung

Assuming a homogeneous interaction probability inside each scintillator layer, the effective measurement depth  $z_n$  of layer  $n$  is taken as the midpoint of the WET interval,

$$z_n = \frac{t_{n-1} + t_n}{2}. \quad (1.20)$$

Under the same assumption of a uniform distribution, the uncertainty of the measurement depth is given by

$$\sigma_{z_n}^2 = \frac{1}{12} (t_n - t_{n-1})^2. \quad (1.21)$$

**Material Parameters Determination** ### Note: Falls einfache WET Berechnung, hier nur Werte für PbWO<sub>4</sub> herleiten

The material-specific parameters  $\alpha$  and  $p$  for water and the detector components (PbWO<sub>4</sub>, PTFE and aluminum) are used in the conversion of the detector depth to WET. They can be determined empirically by performing an exponential fit to proton range-energy data bortfeld. For liquid water and aluminum, the range-energy reference data were obtained directly from ICRU49. Measured range-energy data for PbWO<sub>4</sub> and PTFE were

not available. Instead, the corresponding range-energy tables were generated using a Geant4 (11.2.1) simulation. For that the QGSP\_BIC\_EMY physics list was used with the electromagnetic physics constructor substituted by G4EmStandardPhysics\_option4. The PTFE membrane is approximated by its core chemical composition of C<sub>2</sub>F<sub>4</sub> chains with a density of 0.35  $\frac{\text{g}}{\text{cm}^3}$  as provided by the vendor. The inbuilt G4\_PbWO<sub>4</sub> was used for the PbWO<sub>4</sub> material definition with a density of 8.28  $\frac{\text{g}}{\text{cm}^3}$ . The accuracy of the simulation was validated by comparing the calculated proton ranges for liquid water against the reference data from ICRU49.

The simulated ranges deviated about 1 % for small energies with the deviation decreasing for increasing energies to about 0.5 %, indicating a good accuracy of the simulation. The resulting range-energy data for PbWO<sub>4</sub> and PTFE were subsequently fitted and their respective  $\alpha$  and  $p$  extracted. The final parameters of all used materials are shown in Table ?? with the corresponding fits illustrated in Figure ??.



figs/rangeenergy.pdf

Figure 1.8: Exponential fits using the range-energy relation bortfeld to range-energy data for protons in liquid H<sub>2</sub>O and solid Al from the ICRU49 and for PbWO<sub>4</sub> and PTFE from a Geant4 simulation.

## 1.13 Range-Energy Simulation Validation

## 1.14 Medical Paper/Heterogeneous Phantom

Lastly, a measurement with a heterogeneous LN300 Gammex phantom was done, shown in Figure ???. The phantom has a thickness of 200 mm, a physical density of  $0.30 \text{ g/cm}^3$  and an electron density relative to water of 0.290 gammexphantom. The LN300 phantom has a modulation power of  $210 \mu\text{m}$ , which was measured using a PTW PeakFinder.



Figure 1.9: Heterogeneous phantom setup: 200 mm Gammex LN300 lung equivalent phantom.

Two approaches are presented to analyze the depth dose spectra and extract the modula-

Table 1.2: Fitted material parameters  $\alpha$  and  $p$  using the range-energy relation bortfeld and the range-energy data from ICRU49 and a Geant4 simulation.

Material	$\alpha / \frac{\text{mm}}{\text{MeV}^p}$	$p$	$\text{Cov}(\alpha, p)$
PbWO <sub>4</sub>	$7.275 \times 10^{-3} \pm 1.497 \times 10^{-4}$	$1.69 \pm 3.865 \times 10^{-3}$	$-5.781 \times 10^{-7}$
PTFE	$9.158 \times 10^{-2} \pm 2.387 \times 10^{-3}$	$1.734 \pm 4.890 \times 10^{-3}$	$-1.166 \times 10^{-5}$
Water	$2.585 \times 10^{-2} \pm 6.826 \times 10^{-4}$	$1.738 \pm 4.953 \times 10^{-3}$	$-3.377 \times 10^{-6}$
Aluminum	$1.319 \times 10^{-2} \pm 3.224 \times 10^{-4}$	$1.725 \pm 4.588 \times 10^{-3}$	$-1.477 \times 10^{-6}$

Table 1.3: Measured proton CSDA range ICRU49 and simulated range in H<sub>2</sub>O, PbWO<sub>4</sub>, PTFE and aluminum for various energies. The deviation between measured and simulated range in H<sub>2</sub>O is also given.

Energy [MeV]	ICRU range in H <sub>2</sub> O [mm]	Simulated range in H <sub>2</sub> O [mm]	Deviation [%]	ICRU range in Al [mm]	Simulated range in PbWO <sub>4</sub> [mm]	Simulated range in PTFE [mm]
3	$1.50 \times 10^{-1} \pm 2.25 \times 10^{-3}$	$1.51 \times 10^{-1} \pm 2.28 \times 10^{-3}$	0.589	$8.13 \times 10^{-2} \pm 1.22 \times 10^{-3}$	$5.08 \times 10^{-2} \pm 1.05 \times 10^{-3}$	$8.78 \times 10^{-2} \pm 2.49 \times 10^{-3}$
5	$3.62 \times 10^{-1} \pm 5.43 \times 10^{-3}$	$3.65 \times 10^{-1} \pm 4.64 \times 10^{-3}$	0.636	$1.91 \times 10^{-1} \pm 2.87 \times 10^{-3}$	$1.13 \times 10^{-1} \pm 1.16 \times 10^{-3}$	$2.09 \times 10^{-1} \pm 1.93 \times 10^{-3}$
10	$1.23 \pm 1.84 \times 10^{-2}$	$1.24 \pm 1.61 \times 10^{-2}$	0.714	$6.29 \times 10^{-1} \pm 9.43 \times 10^{-3}$	$3.42 \times 10^{-1} \pm 4.92 \times 10^{-3}$	$6.98 \times 10^{-1} \pm 8.07 \times 10^{-3}$
15	$2.54 \pm 3.81 \times 10^{-2}$	$2.56 \pm 3.27 \times 10^{-2}$	0.750	$1.28 \pm 1.92 \times 10^{-2}$	$6.68 \times 10^{-1} \pm 9.74 \times 10^{-3}$	$1.43 \pm 1.70 \times 10^{-2}$
20	$4.26 \pm 6.39 \times 10^{-2}$	$4.30 \pm 5.28 \times 10^{-2}$	1.027	$2.12 \pm 3.18 \times 10^{-2}$	$1.09 \pm 1.57 \times 10^{-2}$	$2.39 \pm 2.86 \times 10^{-2}$
30	$8.85 \pm 1.33 \times 10^{-1}$	$8.95 \pm 1.05 \times 10^{-1}$	1.047	$4.35 \pm 6.53 \times 10^{-2}$	$2.17 \pm 3.08 \times 10^{-2}$	$4.94 \pm 5.85 \times 10^{-2}$
40	$1.49 \times 10^1 \pm 2.23 \times 10^{-1}$	$1.50 \times 10^1 \pm 1.74 \times 10^{-1}$	0.877	$7.27 \pm 1.09 \times 10^{-1}$	$3.56 \pm 4.68 \times 10^{-2}$	$8.27 \pm 9.71 \times 10^{-2}$
50	$2.23 \times 10^1 \pm 3.34 \times 10^{-1}$	$2.24 \times 10^1 \pm 2.52 \times 10^{-1}$	0.806	$1.08 \times 10^1 \pm 1.62 \times 10^{-1}$	$5.26 \pm 6.51 \times 10^{-2}$	$1.24 \times 10^1 \pm 1.44 \times 10^{-1}$
60	$3.09 \times 10^1 \pm 4.64 \times 10^{-1}$	$3.12 \times 10^1 \pm 3.50 \times 10^{-1}$	0.727	$1.50 \times 10^1 \pm 2.24 \times 10^{-1}$	$7.21 \pm 8.62 \times 10^{-2}$	$1.71 \times 10^1 \pm 1.97 \times 10^{-1}$
70	$4.08 \times 10^1 \pm 6.12 \times 10^{-1}$	$4.11 \times 10^1 \pm 4.61 \times 10^{-1}$	0.671	$1.97 \times 10^1 \pm 2.95 \times 10^{-1}$	$9.42 \pm 1.10 \times 10^{-1}$	$2.26 \times 10^1 \pm 2.58 \times 10^{-1}$
80	$5.18 \times 10^1 \pm 7.78 \times 10^{-1}$	$5.22 \times 10^1 \pm 5.79 \times 10^{-1}$	0.627	$2.49 \times 10^1 \pm 3.74 \times 10^{-1}$	$1.19 \times 10^1 \pm 1.36 \times 10^{-1}$	$2.86 \times 10^1 \pm 3.24 \times 10^{-1}$
90	$6.40 \times 10^1 \pm 9.60 \times 10^{-1}$	$6.44 \times 10^1 \pm 7.10 \times 10^{-1}$	0.600	$3.07 \times 10^1 \pm 4.60 \times 10^{-1}$	$1.45 \times 10^1 \pm 1.65 \times 10^{-1}$	$3.53 \times 10^1 \pm 3.96 \times 10^{-1}$
100	$7.72 \times 10^1 \pm 1.16$	$7.76 \times 10^1 \pm 8.57 \times 10^{-1}$	0.580	$3.70 \times 10^1 \pm 5.54 \times 10^{-1}$	$1.74 \times 10^1 \pm 1.95 \times 10^{-1}$	$4.26 \times 10^1 \pm 4.72 \times 10^{-1}$
125	$1.15 \times 10^2 \pm 1.72$	$1.15 \times 10^2 \pm 1.26$	0.536	$5.47 \times 10^1 \pm 8.20 \times 10^{-1}$	$2.56 \times 10^1 \pm 2.81 \times 10^{-1}$	$6.31 \times 10^1 \pm 6.90 \times 10^{-1}$
150	$1.58 \times 10^2 \pm 2.37$	$1.59 \times 10^2 \pm 1.69$	0.607	$7.51 \times 10^1 \pm 1.13$	$3.49 \times 10^1 \pm 3.79 \times 10^{-1}$	$8.68 \times 10^1 \pm 9.35 \times 10^{-1}$
175	$2.06 \times 10^2 \pm 3.09$	$2.07 \times 10^2 \pm 2.20$	0.569	$9.80 \times 10^1 \pm 1.47$	$4.52 \times 10^1 \pm 4.87 \times 10^{-1}$	$1.13 \times 10^2 \pm 1.20$
200	$2.60 \times 10^2 \pm 3.89$	$2.61 \times 10^2 \pm 2.74$	0.501	$1.23 \times 10^2 \pm 1.85$	$5.66 \times 10^1 \pm 6.08 \times 10^{-1}$	$1.43 \times 10^2 \pm 1.51$
225	$3.17 \times 10^2 \pm 4.76$	$3.19 \times 10^2 \pm 3.33$	0.500	$1.50 \times 10^2 \pm 2.25$	$6.89 \times 10^1 \pm 7.37 \times 10^{-1}$	$1.74 \times 10^2 \pm 1.87$
250	$3.79 \times 10^2 \pm 5.69$	$3.81 \times 10^2 \pm 3.98$	0.490	$1.79 \times 10^2 \pm 2.69$	$8.20 \times 10^1 \pm 8.68 \times 10^{-1}$	$2.08 \times 10^2 \pm 2.29$

tion power. The first is the standard convolution of a linear interpolated reference curve and fitting the result to the depth dose spectra of the heterogeneous phantom Baumann2017. The second approach

$$D(z) = (\hat{D} * \mathcal{N})(z) = \frac{1}{\sqrt{2\pi}\sigma} \int_{-\infty}^{R_0} \hat{D}(\bar{z}) e^{-\frac{(z-\bar{z})^2}{2\sigma^2}} d\bar{z} \quad (1.22)$$

$$= \Phi_0 \frac{e^{-\zeta^2/4} \sigma^{1/p} \Gamma(1/p)}{\sqrt{2\pi\rho p \alpha^{1/p} (1 + \beta R_0)}} \cdot \left[ \frac{1}{\sigma} \mathcal{D}_{-1/p}(-\zeta) + \left( \frac{\beta}{p} + \gamma\beta + \frac{\epsilon}{R_0} \right) \mathcal{D}_{-1/p-1}(-\zeta) \right], \quad \zeta = \frac{R_0 - z}{\sigma} \quad (1.23)$$

We start from the pre-convolved depth dose distribution, shown in Equation ??, which is given as the depth dose distribution without range straggling  $\hat{D}$  convolution with a range straggling normal distribution  $\mathcal{N}$ . The depth dose distribution after passing a heterogeneous phantom  $D_h(z; t, \sigma_t)$  is calculated by performing a second convolution with a normal distribution  $\mathcal{N}_t$ , where the displacement  $t$  and broadening  $\sigma_t$  are the parameters of the modulation power. Using the associativity of convolutions, we first convolve the two normal distributions, giving a single normal distribution  $\mathcal{N}_h$  with standard deviation  $\sigma_h = \sqrt{\sigma^2 + \sigma_t^2}$  and mean  $\mu_h = z - t$ . From there, we shift the integral limit by  $t$  and change the fluence normalization to account for the changed range  $R_t = R_0 - t$  by defining  $\Phi'_0$  as the fluence after the heterogeneous target with  $\frac{1+\beta(R_0-t)}{1+\beta R_0}$  being the fluence reduction factor. This results in the final depth dose distribution for the heterogeneous phantom shown in Equation ??, which has the same form as the depth dose distribution without a target except that the range  $R_0$  is reduced by the displacement  $t$ , the width  $\sigma$  is broadened according to the quadrature sum of the two individual widths and the fluence  $\Phi_0$  is adjusted by the lost particles in the phantom to  $\Phi'_0$ .

$$D_h(z; t, \sigma_t) = (\hat{D} * \mathcal{N} * \mathcal{N}_t)(z) = (\hat{D} * \mathcal{N}_h)(z) \quad (1.24)$$

$$= \frac{1}{\sqrt{2\pi}\sigma_h} \int_{-\infty}^{R_0} \hat{D}(\bar{z}) e^{-\frac{(z-t-\bar{z})^2}{2\sigma_h^2}} d\bar{z} \quad (1.25)$$

$$= \frac{1}{\sqrt{2\pi}\sigma_h} \int_{-\infty}^{R_0-t} \hat{D}(\tilde{z}-t) e^{-\frac{(z-\tilde{z})^2}{2\sigma_h^2}} d\tilde{z} \quad (1.26)$$

$$= \Phi'_0 \frac{e^{-\zeta'^2/4} \sigma_h^{1/p} \Gamma(1/p)}{\sqrt{2\pi} \rho p \alpha^{1/p} (1 + \beta R_t)} \cdot \left[ \frac{1}{\sigma_h} \mathcal{D}_{-1/p}(-\zeta') + \left( \frac{\beta}{p} + \gamma \beta + \frac{\varepsilon}{R_t} \right) \mathcal{D}_{-1/p-1}(-\zeta') \right], \quad \zeta' = \frac{R_t - z}{\sigma_h} \quad (1.27)$$

$$= D(z; R_t = R_0 - t, \sigma_h = \sqrt{\sigma^2 + \sigma_t^2}, \Phi'_0 = \Phi_0 \frac{1 + \beta(R_0 - t)}{1 + \beta R_0}) \quad (1.28)$$

figs/bragghet.pdf

Figure 1.10: Depth-dose measurements and fits of measurements without a phantom and with a heterogeneous LN300 phantom.

The mean nominal LN300 phantom thickness  $t_{\text{nominal}}$  can be calculated from the electron density ratio to water of 0.28 to 5.8 cm. The measured value of  $5.836 \pm 0.018$  cm agrees with this within 0.56 %, corresponding to an absolute deviation of 360  $\mu\text{m}$ . The

measured modulation power agrees with the nominal value within 2.64 %, corresponding to an absolute deviation of 5.541  $\mu\text{m}$ .

Table 1.4: Fit results obtained from depth-dose distributions measured without a phantom and with the heterogeneous LN300 phantoms. From left to right: the range of the distal fall-off  $R_0$ , the width of the Bragg peak or range and energy straggling  $\sigma$ , the reconstructed WET of the LN300 phantom from range difference to the measurement without a target  $t$ , the modulation Power  $P_{\text{mod}}$ , the nominal  $P_{\text{mod,nom.}}$ , the absolute deviation  $\Delta P = P_{\text{mod}} - P_{\text{mod,nom.}}$  and the relative deviation  $\Delta P\%$ . The deviations are given with respect to the nominal modulation power  $P_{\text{mod,nom.}}$ , measured using a PTW peakfinder.

Phantom	$R_0 / \text{cm}$	$\sigma / \text{cm}$	$t / \text{cm}$	$P_{\text{mod}} / \mu\text{m}$	$P_{\text{mod,nom.}} / \mu\text{m}$	$\Delta t / \mu\text{m}$
None	$30.991 \pm 0.002$	$0.489 \pm 0.004$	-	-	-	-
LN300	$25.156 \pm 0.018$	$0.604 \pm 0.028$	$5.836 \pm 0.018$	$215.541 \pm 9.886$	210	5.541

# Bibliography

- [1] JLU Giessen R. Schubert. *Personal communication*. 2024.
- [2] Hamamatsu Photonics. *R1828-01, R2059 Photomultiplier Tubes Datasheet*. Accessed: 2024-10-28. Hamamatsu Photonics K.K. 2019. URL: [https://www.hamamatsu.com/content/dam/hamamatsu-photonics/sites/documents/99%5C\\_SALES%5C\\_LIBRARY/etd/R1828-01%5C\\_R2059%5C TPMH1259E.pdf](https://www.hamamatsu.com/content/dam/hamamatsu-photonics/sites/documents/99%5C_SALES%5C_LIBRARY/etd/R1828-01%5C_R2059%5C TPMH1259E.pdf).
- [3] *The CMS electromagnetic calorimeter project: Technical Design Report*. Technical design report. CMS. Geneva: CERN, 1997. URL: <https://cds.cern.ch/record/349375>.
- [4] Bayer AG. *Baysilone® Fluids Brochure*. Accessed: 2024-10-30. 2020. URL: <https://dcproducts.com.au/wp-content/uploads/2020/12/BayerBaysiloneFluidsBrochure.pdf>.
- [5] I. H. Malitson. “Interspecimen Comparison of the Refractive Index of Fused Silica”. In: *J. Opt. Soc. Am.* 55 (Oct. 1965). DOI: 10.1364/JOSA.55.001205.

# **List of Figures**

# **List of Tables**

## Selbstständigkeitserklärung

Hiermit versichere ich, die vorgelegte Thesis selbstständig und ohne unerlaubte fremde Hilfe und nur mit den Hilfen angefertigt zu haben, die ich in der Thesis angegeben habe. Alle Textstellen, die wörtlich oder sinngemäß aus veröffentlichten Schriften entnommen sind, und alle Angaben die auf mündlichen Auskünften beruhen, sind als solche kenntlich gemacht. Bei den von mir durchgeführten und in der Thesis erwähnten Untersuchungen habe ich die Grundsätze gute wissenschaftlicher Praxis, wie sie in der ‚Satzung der Justus-Liebig-Universität zur Sicherung guter wissenschaftlicher Praxis‘ niedergelegt sind, eingehalten. Entsprechend § 22 Abs. 2 der Allgemeinen Bestimmungen für modularisierte Studiengänge dulde ich eine Überprüfung der Thesis mittels Anti-Plagiatssoftware.

---

Datum

---

Unterschrift